Journal of Pathology
J Pathol October 2021; **255:** 190–201
Published online 5 August 2021 in Wiley Online Library (wileyonlinelibrary.com) DOI: 10.1002/path.5753

ORIGINAL PAPER

Heterogenous presence of neutrophil extracellular traps in human solid tumours is partially dependent on IL-8

Carlos E de Andrea[1,2,3†], María Carmen Ochoa[3,4†], María Villalba-Esparza[1,3†], Álvaro Teijeira[3,4,5], Kurt A Schalper[6], Marta Abengozar-Muela[1,2], Iñaki Eguren-Santamaría[7,4], Cristina Sainz[1], Sandra Sánchez-Gregorio[4], Saray Garasa[4,5], Mikel Ariz[3,5], Carlos Ortiz-de-Solorzano[3,5], María E Rodriguez-Ruiz[4,7], Jose L Perez-Gracia[7], María D Lozano[1,2], José I Echeveste[1,2], Miguel F Sanmamed[3,4,5,7‡] and Ignacio Melero[3,4,5‡*]

[1] *Department of Pathology, Clínica Universidad de Navarra, Pamplona, Spain*
[2] *Department of Anatomy, Physiology and Pathology, University of Navarra, Pamplona, Spain*
[3] *Centro de Investigación Biomédica en Red de Cáncer (CIBERONC), Madrid, Spain*
[4] *Division of Immunology and Immunotherapy, Center for Applied Medical Research (CIMA), University of Navarra, Pamplona, Spain*
[5] *Navarra Institute for Health Research (IdISNA), Pamplona, Spain*
[6] *Department of Pathology, Yale University School of Medicine, New Haven, CT, USA*
[7] *Department of Oncology, Clínica Universidad de Navarra, Pamplona, Spain*

**Correspondence to: I Melero, Immunology and Immunotherapy Department, CIMA, Avda Pio XII, 55, 31008 Pamplona, Spain. E-mail: imelero@unav.es*

[†]These authors contributed equally
[‡]Co-senior authors

Abstract

Neutrophil extracellular traps (NETs) are webs of extracellular nuclear DNA extruded by dying neutrophils infiltrating tissue. NETs constitute a defence mechanism to entrap and kill fungi and bacteria. Tumours induce the formation of NETs to the advantage of the malignancy via a variety of mechanisms shown in mouse models. Here, we investigated the presence of NETs in a variety of human solid tumours and their association with IL-8 (CXCL8) protein expression and $CD8^+$ T-cell density in the tumour microenvironment. Multiplex immunofluorescence panels were developed to identify NETs in human cancer tissues by co-staining with the granulocyte marker CD15, the neutrophil marker myeloperoxidase and citrullinated histone H3 (H3Cit), as well as IL-8 protein and $CD8^+$ T cells. Three ELISA methods to detect and quantify circulating NETs in serum were optimised and utilised. Whole tumour sections and tissue microarrays from patients with non-small cell lung cancer (NSCLC; $n = 14$), bladder cancer ($n = 14$), melanoma ($n = 11$), breast cancer ($n = 31$), colorectal cancer ($n = 20$) and mesothelioma ($n = 61$) were studied. Also, serum samples collected retrospectively from patients with metastatic melanoma ($n = 12$) and NSCLC ($n = 34$) were ELISA assayed to quantify circulating NETs and IL-8. NETs were detected in six different human cancer types with wide individual variation in terms of tissue density and distribution. At least in NSCLC, bladder cancer and metastatic melanoma, NET density positively correlated with IL-8 protein expression and inversely correlated with $CD8^+$ T-cell densities. In a series of serum samples from melanoma and NSCLC patients, a positive correlation between circulating NETs and IL-8 was found. In conclusion, NETs are detectable in formalin-fixed human biopsy samples from solid tumours and in the circulation of cancer patients with a considerable degree of individual variation. NETs show a positive association with IL-8 and a trend towards a negative association with $CD8^+$ tumour-infiltrating lymphocytes.

Keywords: NETs; neutrophil extracellular traps; neutrophils forming NETs; neutrophils; IL-8; CXCR1/CXCR2; solid tumour

Received 7 March 2021; Revised 17 May 2021; Accepted 23 June 2021

Conflict of interest statement: IM reports receiving commercial research grants from Bristol Myers Squibb, Bioncotech, Alligator, Pfizer, Leadartis and Roche, has received speakers bureau honoraria from MSD and is a consultant or advisory board member for Bristol Myers Squibb, Roche, Genmab, F-Star, Bioncotech, Bayer, Numab, Pieris, Alligator and Merck Serono. MFS reports research grants from Roche. JLPG reports research grants and support from Roche, Bristol Myers Squibb, MSD, Ipsen, Eisai, Incyte, Janssen, Seattle Genetics; speakers bureau honoraria and advisory boards from Roche, Bristol Myers Squibb, Ipsen, MSD, Seattle Genetics; and travel support from Roche, MSD, Bristol Myers Squibb. CEA reports research grants from AstraZeneca. MERR reports receiving research grants from Bioncotech, and Roche; has received speakers bureau honoraria from Bristol Myers Squibb and ROCHE; and travel support from Roche, Bristol Myers Squibb and AstraZeneca. KAS reports receiving research funding from Genoptix/Navigate (Novartis), Tesaro, Moderna Therapeutics, Takeda, Surface Oncology, Pierre-Fabre Research Institute, Merck, Bristol Myers Squibb, AstraZeneca and Eli Lilly; KAS has received honoraria for consultant/advisory roles from Celgene, Moderna Therapeutics, Shattuck Labs, Pierre-Fabre, AstraZeneca, EMD Serono, Ono Pharmaceuticals, Clinica Alemana de Santiago, Dynamo Therapeutics, PeerView, Abbvie, Fluidigm, Takeda/Millenium Pharmaceuticals, Merck, Bristol Myers Squibb, Agenus and Torque Therapeutics. All other authors declared no conflicts of interest.

Introduction

Neutrophils are critical in the defence against extracellular bacteria and fungi. One of their antimicrobial mechanisms is a form of cell death upon which neutrophils extrude nuclear DNA coated with granular and cytoplasmic proteins, including bactericidal polypeptides and proteases [1,2]. Such extracellular DNA webs are called neutrophil extracellular traps (NETs) and the process of cell death is termed NETosis [3].

In addition to their role as a defence mechanism to entrap and kill prokaryotic microbes, NETs have been involved in the pathogenesis of a wide variety of human conditions, including thrombosis [4], gout [5] and biliary lithiasis [6], among others [7]. Cancer-associated thrombosis reportedly has a NET component [8].

In mouse models of cancer, NETs are formed and diverse experimental tools have documented a role in fostering metastasis [9,10], awakening tumour dormancy [11,12] and mediating suppression of antitumour cytotoxic immune cells [13]. NETosis can be induced by a variety of agents and proinflammatory mediators. Importantly, these include CXCL ELR$^+$ chemokines that are abundantly produced in tumour tissue microenvironments [13,14]. In human cancer, CXCL8 (IL-8) seems to be the most copiously CXCL ELR$^+$ present chemokine [15]. IL-8 not only induces NETosis when present in relatively high concentrations, but also seems to be the most prominent chemoattractant for neutrophils in humans [16,17]. Neutrophils and myeloid-derived suppressor cells exert protumour activities, largely by inducing interference with antitumour immunity, although neutrophils may also mediate some anticancer actions [15,18].

The importance of NETs in human malignancies is beginning to emerge. B-cell lymphoma patients show increased circulating levels of NETs that correlate with serum IL-8 and worse prognosis [19]. Moreover, reports suggest the presence of NETs in pancreatic, gastric and ovarian cancer, where they correlate with worse prognosis [20–23]. However, accurate analytical studies supporting reliable measurement of NETs are needed [20,23].

Here, we developed a multiplexed immunofluorescence assay to measure NETs and neutrophils forming NETs in formalin-fixed human biopsy tissue and use it to demonstrate the levels and distribution of NETs in multiple human solid tumours. NETs become evident upon co-staining with the granulocyte marker CD15, the neutrophil marker myeloperoxidase (MPO) and citrullinated histone H3 (H3Cit). Each of these markers alone can also be detected in other cells and processes. For instance, MPO could be expressed by activated macrophages [24] and histone 3 citrullination also occurs in chromatin decondensation during mitosis. Furthermore, three ELISA methods show the variable presence of NETs in circulation. IL-8 abundance in tissue or serum has been found to correlate to some extent with the amount of NETs, consistent with the potent induction of NETs by IL-8 [19].

NETosis can be therapeutically blocked at different levels. IL-8 can be neutralised with monoclonal antibodies and CXCR1/2 inhibitors are undergoing clinical trials [25,26]. Moreover, NETosis is critically contingent upon histone H3 citrullination by the enzyme PAD-4 and selective inhibitors of PAD-4 are under development [27]. Additionally, extracellular DNA can be degraded by DNAse I, which is available at GMP-grade [28]. Therefore, the dynamic evaluation of NETs in tissue and in serum could support their possible use as biomarkers.

Materials and methods

Patients, cohorts and tissue microarrays

Formalin-fixed, paraffin-embedded (FFPE) samples from retrospective collections of non-small cell lung cancer (NSCLC), bladder cancer, breast cancer, colorectal cancer (CRC) and mesothelioma presented in tissue microarrays (TMA) were analysed. In addition, whole tissue sections from metastatic melanomas were studied. The NSCLC, bladder cancer, breast cancer and CRC collections (in total or partially) have been reported previously [29–31]. The tissue collections included samples seen at the Pathology Department of the Clínica Universidad de Navarra (Pamplona, Spain) from 14 patients with NSCLC, 14 patients with bladder cancer, 31 patients with breast cancer, 20 patients with CRC, 61 patients with mesothelioma and 11 patients with metastatic melanoma. All tissue was used after approval from the Universidad de Navarra Human Investigation Committee, protocol numbers: 2010.111 mod4, 2019.012, 2019.180, 111/2010, 2019-76 and 2019.084. All cases were reviewed by trained pathologists using H&E-stained slides and the tumour histology variant was confirmed by morphological analysis. TMAs were prepared using standard procedures, as described previously [32]. In brief, after pathology review of H&E-stained slides, 1 mm cores were obtained from the original paraffin blocks using a needle and inserted into a recipient paraffin block. For better representation of the tumours, two cores obtained from different areas were included in the TMAs. Clinicopathological information from all patients was collected from clinical records and pathology reports and is detailed in supplementary material, Table S1.

ELISAs

Blood samples were obtained by venipuncture from patients with melanoma and NSCLC under specimen repository protocol from our institution (protocol number 111/2010). Cell-free serum samples were aliquoted and immediately stored at −80 °C.

IL-8 levels were quantified using a commercially purchased ELISA kit used according to the manufacturer's instructions (product # 555244, BD Biosciences, Heidelberg, Germany).

Indirect quantification of NETs in serum was carried out by determining the MPO–DNA complexes, H3Cit and the MPO–histone H3 complexes. Those three different assays provided quantitative data related to the concentration of NETs in serum and the results of these measurements were correlated with each other (see supplementary material, Figure S1A,B) Levels of H3Cit were measured with the Cayman Chemical ELISA kit (product # 501620, Cayman Chemical, Ann Arbor, MI, USA).

MPO–histone H3 complexes were measured in a similar sandwich approach. In this case, the capturing antibody was also the anti-MPO monoclonal antibody that was also coated onto 96-well microtitre plates overnight at 4 °C. After blocking in 1% BSA for 1 h, patient serum diluted 1:4 in 1% BSA was added. After incubation for 2 h at room temperature on a shaking device, the samples were washed seven times with 0.1% Tween 20 in PBS and incubated for 1 h with the HRP-conjugated anti-histone H3 antibody taken from the Cayman Chemical kit (Cayman Chemical). Then, samples were washed and developed in the same way as the MPO–DNA complexes. As standards, NETs isolated from supernatants from IL-8 activated neutrophils were used. In this case, the standard curve values were adjusted to a one phase decay model with an $r > 0.98$ to extrapolate (U/ml) from the absorbance values of the samples.

In vitro NET production

Neutrophils were isolated from peripheral blood from a volunteer blood donor database of young adults (male and female) mainly composed of undergraduate students of the Universidad de Navarra (Pamplona, Spain). Written, signed and dated informed consent was obtained according to a protocol approved by the Institutional Ethical Committee, as described earlier (protocol number 2019-76). Neutrophils were resuspended in HBSS (Gibco, Life Technologies, Stockholm, Sweden) and plated in six-well plates at a concentration of 2×10^6 cells per 1.5 ml. Neutrophils were stimulated with 1 mg/ml PMA (Sigma-Aldrich, St Louis, MO, USA) or 100 ng/ml CXCL8 (product # 130-093-943, Miltenyi Biotec, Bergisch Gladbach, Germany). After incubation for 4 h at 37 °C in 5% CO_2, cells were recovered with cold Dulbecco's PBS (Sigma-Aldrich) and centrifuged at 4 °C, 10 000 × *g* for 10 min, inhibiting further stimulation. Cells were fixed with 4% formaldehyde overnight and then centrifuged again. The supernatant was discarded and the pellet was stained with haematoxylin and then embedded in paraffin wax.

Multiplexed immunofluorescence staining

The validation pipeline and details of the multiplex immunolabelling protocol development have been described previously by our group [33,34]. A six-colour multiplex quantitative immunofluorescence protocol for FFPE tissue specimens was developed for simultaneous detection of DAPI, CD15, MPO, H3Cit, CD8 and cytokeratin using isotype-specific antibodies and different fluorescence conjugates. To reliably measure the markers, we first validated single-plex assays using human phlegmonous appendicitis and lung abscess, and NSCLC tissues (Figure 1A–C). The single-plex assays were used as the gold standard for cell antigen visualisation. The markers were then integrated into a multiplexed immunofluorescence panel. Therefore, each single antibody was optimised individually for its optimal conditions and position in the sequence of multiplex staining. A single-plex versus multiplex comparison for each antibody was carried out to validate the staining patterns and distribution. Based on this comparison, we established the optimal signal through dilution of the primary antibodies and/or the fluorophores to obtain staining levels and cell counts comparable with conventional single-plex immunofluorescence staining (Figure 1A–C).

For the multiplexed staining, sections were deparaffinised and subjected to four sequential rounds of antibody staining. Antigen retrieval was carried out using DAKO PT-Link (Dako, Glostrup, Denmark) heat-induced antigen retrieval with low pH (pH 6) or high pH (pH 9) target retrieval solution (Dako). The first round consisted of antigen retrieval with low pH (pH 6), protein blocking with antibody diluent/block (Akoya Bioscience, Menlo Park, CA, USA), incubation with anti-histone H3 (citrulline R2+R8+R17, H3Cit, green) antibody (rabbit polyclonal, 1:100, product # ab5103; Abcam, Cambridge, MA, USA), biotinylated anti-mouse/rabbit secondary antibodies and streptavidin-HRP (product # 50003, Dako), followed by tyramide signal amplification (TSA) visualisation with fluorophore Opal 690 (Akoya Biosciences). The second round comprised similar steps but using antigen retrieval with high pH (pH 9), incubation with CD15 (mouse monoclonal, clone Carb-3, 1:100, product # IR062; Agilent, Santa Clara, CA, USA) and TSA visualisation with fluorophore Opal 620 (Akoya Biosciences). The third round consisted of antigen retrieval with EDTA, protein blocking with 0.3% BSA in 0.05% Tween 20 (ThermoFisher Scientific, Dreieich, Germany) and incubation overnight at 4 °C with CD8 (mouse monoclonal, clone C8/144B, isotype IgG1, kappa, ready-to-use, product # IR623, Agilent) and MPO (rabbit monoclonal, clone E1E7I, isotype IgG, 1:2,000, product # 14569S, Cell Signaling Technology, Beverly, MA, USA), followed by incubation with rabbit Envision secondary antibody and visualisation with Cy5 tyramide (1:50, Perkin Elmer, Waltham, MA, USA), anti-mouse IgG1 (1:100, product # ab18-4010-82, eBioscience/Affymetrix, San Diego, CA, USA) and Cy3 tyramide Plus (1:100, Perkin Elmer). A solution of benzoic hydrazide (100 mM) and hydrogen peroxide (50 mM) was used to block residual HRP enzyme activity after each tyramide incubation. Sections were then incubated with polyclonal rabbit anti-cytokeratin, wide spectrum screening, (1:100, product # Z0622, Agilent) and the secondary antibody goat anti-rabbit Alexa488. Finally, nuclei were counterstained with spectral DAPI (Akoya Bioscience) and sections were mounted with Faramount Aqueous Mounting Medium (Dako).

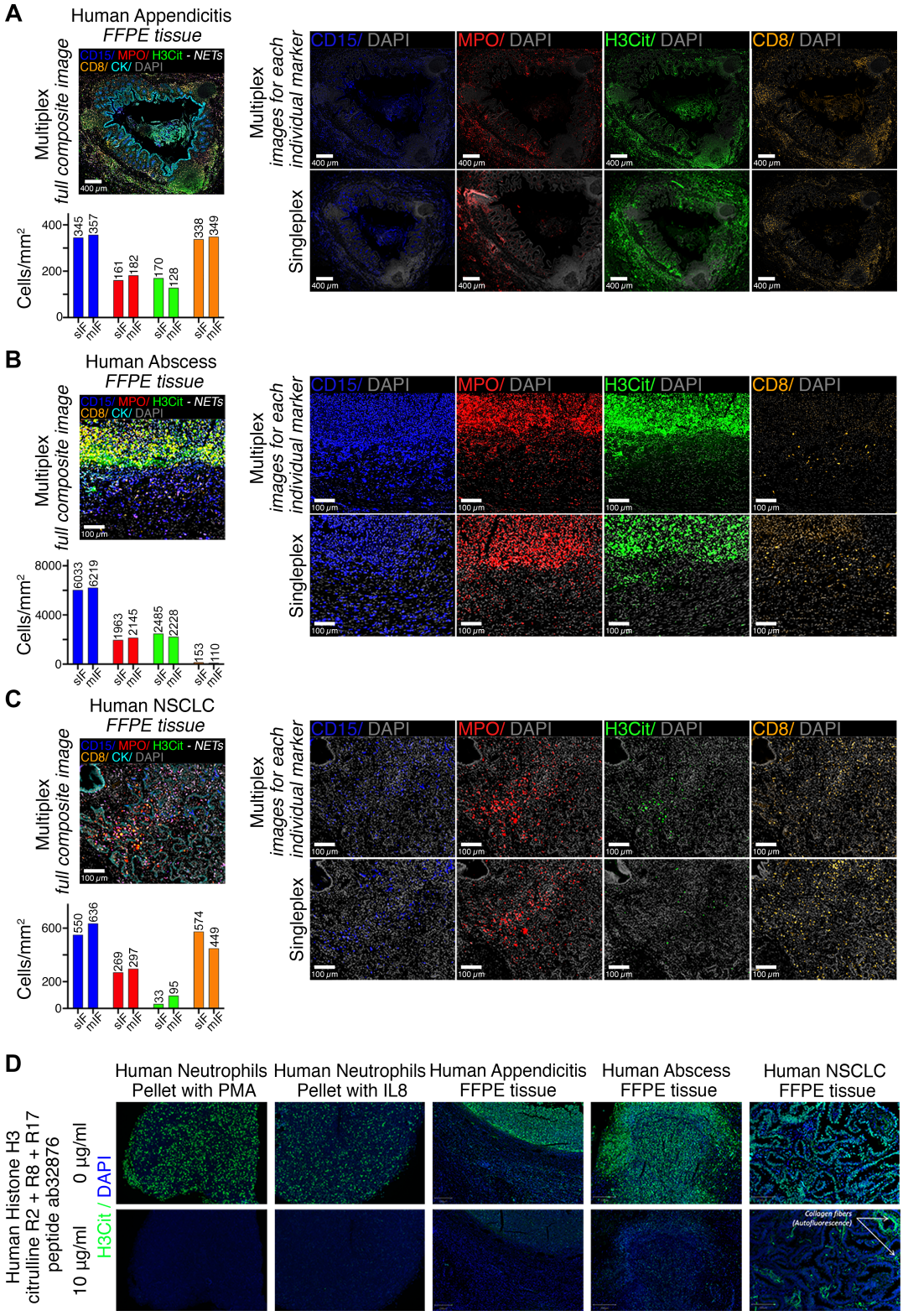

Figure 1. Multiplex staining protocols and validation workflow for NET detection. (A–C) Spectrally unmixed composite image of FFPE tissue sections from human phlegmonous appendicitis, lung abscess and NSCLC stained for CD15 (clone Carb-3, blue), MPO (clone E1E7I, red), anti-histone H3 (citrulline R2+R8+R17, H3Cit, green), CD8 (clone C8/144B, red), cytokeratin (wide spectrum screening, cyan) and DAPI (grey). Images for each of the individual markers and marker combinations used to identify NETs ($CD15^+$, MPO^+, $H3Cit^+$) are shown. NETs are visualised as white structures in the full composite colour images. Multiplex immunofluorescence (mIF) images were compared against corresponding fluorescent channels from single-plex immunofluorescence (sIF) images from sequential tissue sections (bar charts). The total number of cells for each marker comparing sIF against the corresponding fluorescent channel from mIF on sequential FFPE sections was used to optimise the six-colour multiplex immunolabelling protocol. (D) Peptide competition assay in cell pellets from neutrophils activated with PMA or IL-8 to form NETs and tissue sections from cases of appendicitis, abscess and NSCLC. The upper panel shows the mock incubation; the lower panel represents the antibody block at 10 µg/ml with the peptide (ab32876). Scale bars: A, 400 µm; B,C, 100 µm.

For IL-8 immunofluorescence staining, a four-colour quantitative immunofluorescence protocol for FFPE tissue specimens was developed for simultaneous detection of DAPI, IL-8, MPO, cytokeratin and different fluorescence conjugates, as described previously by our team [35]. Primary antibodies included IL-8 (mouse monoclonal, clone 807, 1:5000, product # ab18672, Abcam), MPO (rabbit monoclonal, clone E1E7I, isotype IgG, 1:2000, product # 14569S, Cell Signaling Technology) and pan-cytokeratin (polyclonal rabbit, 1:100, product # Z0622, Agilent). The secondary antibodies and fluorescent reagents used were: anti-rabbit Envision (product # K4003, Dako) with fluorescein-tyramide (PerkinElmer); anti-mouse IgG2a antibody (Abcam) with Cy3 plus (PerkinElmer); anti-mouse Envision (product # K40001, Dako) with Cy5 tyramide (PerkinElmer).

Tissue imaging, measurement and scoring

TMAs and whole tissue sections were scanned on a Vectra-Polaris Automated Quantitative Pathology Imaging System (Akoya Biosciences). Tissue imaging and spectral unmixing were performed using inForm software (version 2.4.8, Akoya Biosciences), as described previously [33,34]. Image analysis was then carried out on whole TMA spots and whole tumour area using the open-source digital pathology software QuPath version 0.2.3 (University of Edinburgh, Edinburgh, UK; https://qupath.github.io) and ImageJ software version 1.52c (NIH, Bethesda, MD, USA; http:// imagej.nih.gov/ij). In brief, cell segmentation based on nuclear detection was performed using the StarDist 2D algorithm [36]. A random trees algorithm classifier was trained separately for each cell marker by an experienced pathologist (CEA) annotating the tumour regions. Interactive feedback on cell classification performance was provided during training in the form of a markup image, significantly improving the accuracy of machine learning-based phenotyping [37]. Based on the markers, cells were further classified as $CD8^+$ T cells ($CD8^+$) and neutrophils ($CD15^+$/MPO^+ cells). Cells negative for these markers were defined as 'ignored'. Cells close to the border of the images were removed to reduce the risk of staining artefacts or phenotyping errors.

An ImageJ software plugin was developed and validated to reliably identify and measure NETs and neutrophils forming NETs based on the co-staining with CD15, MPO and H3Cit. In brief, Otsu thresholding was applied on each TMA spot and tissue section to establish single threshold levels of detection for each individual marker. This automated thresholding method allowed the detections acquired at different exposure times to be comparable. A median filter with one-pixel radius for denoising and a size filtering for small, noisy particle removal was then applied. The total tissue area was also calculated by the same plugin and used to normalise the area of NETs and calculate the area percentage NETs for each TMA spot and tissue section and tile. The NETs ImageJ plugin was further validated by correlating the NETs and neutrophils forming NETs area percentage from each TMA spot and tissue section with the neutrophil density obtained by the random trees algorithm classifier described above (see supplementary material, Figure S2A–F).

For each whole tissue section of metastatic melanoma, a grid of tiles (250×250 μm^2 per tile) covering the entire tumour tissue was analysed for $CD8^+$ T-cell and neutrophil densities and NETs/neutrophils forming NETs area.

IL-8 protein expression was calculated as described previously by our team [35]. IL-8 was measured by the mean-normalised pixel intensity in the total tissue compartment by collecting the signal score in the area defined by DAPI staining (e.g. all cells in the sample).

Peptide competition

To determine the specificity of the antibody targeted against histone H3 (citrulline R2+R8+R17, product # ab5103, Abcam) a peptide competition assay was carried out. The antibody incubation was replaced with either a mock incubation (with only blocking solution) or antibody preincubated with 1 or 10 µg/ml human histone H3 (citrulline R2+R8+R17) peptide (product # ab32876, Abcam) for 1 h at room temperature in a roller mixer.

Single-plex immunofluorescence against H3Cit was performed on the following positive controls: neutrophil pellets stimulated with PMA or IL-8 as described above; human phlegmonous appendicitis; lung abscess; lung adenocarcinomas. During the primary antibody incubation, the mock solution or preincubated antibody plus competing peptide was added to the slides at 10 µg/ml (in those cases incubated with antibody), as shown in Figure 1D.

Statistical analyses

Scores between targets ($CD8^+$ T-cell and neutrophil densities, NETs area and IL-8 protein expression) were analysed using linear regression, correlation functions and expressed as regression/correlation coefficients. For the retrospective TMA collections including two spots per case, we analysed the mean score for each case. For the correlation of CD8 densities and NETs in each tile area of metastatic melanoma, quartile 1 (tumours with the lowest NETs area percentage) were compared to quartile 4 (tumours with the highest NETs area percentage). Correlation studies were carried out to calculate linear regression coefficients and/or Spearman rho-rank functions. Associations between the markers and statistical significance were determined using GraphPad Prism v7.0a software (Graphpad Software, San Diego, CA, USA).

Results

Detection and quantification of NETs in human tissue

Multiplex tissue immunofluorescence permits simultaneous detection of multiple molecules with tissue spatial

resolution. We reasoned that NETs would be unequivocally identified by co-staining with the granulocyte marker CD15, the neutrophil marker MPO and H3Cit. Such triple staining would not be confounded due to its ability to distinguish NETs from other forms of extracellular DNA. For example, some nuclei of tumour cells also seem to be characterised by H3Cit staining [38] and macrophages may express MPO [39].

Using profusely NET-infiltrated phlegmonous appendicitis tissue, triple NET staining ($CD15^+/MPO^+/H3Cit^+$) was shown (Figure 1A). We added CD8 staining to the multiplex panel, as we had hypothesised that $CD8^+$ T lymphocytes might be negatively impacted by neutrophils and NETs [13,35]. Such findings were further confirmed in a surgically excised human lung abscess (Figure 1B).

The new methodology could be used in cancer tissue, as in sections of NSCLC adenocarcinoma with abundant neutrophils and $CD8^+$ T cells, multiplex immunofluorescence offered clear-cut quantitative results (Figure 1C).

Each of the antibodies was validated by single-plex immunofluorescence staining and showed similar quantitative results (bar charts in Figure 1A–C). Nonetheless, the specificity of the anti- H3Cit was further confirmed to exclude cross-reactivity or non-specific staining. Figure 1D shows that competition with the immunising peptide to generate the anti-histone H3 polyclonal antibody wholly abrogated the staining, except in the areas of autofluorescence. We also documented that some tumour cells showed nuclear staining for H3Cit, perhaps as a result of mitosis. However, triple staining ($CD15^+/MPO^+/H3Cit^+$) results offered a quantitative estimation of NETs formed by neutrophils.

Multiple human cancer types contain NETs with individual heterogeneity

Using the multiplex immunofluorescence panel to detect and quantitate NETs and neutrophils forming NETs, we stained a series of TMAs derived from a collection of NSCLC (10 adenocarcinomas and four squamous cell carcinomas), bladder cancer ($n = 14$), breast cancer ($n = 31$), CRC ($n = 20$) and mesothelioma ($n = 61$). Furthermore, 11 cases of metastatic melanoma resections were included in the study (see supplementary material, Table S1). Overall, our data indicated the unequivocal presence of NETs in at least a fraction of the examined cases (Figure 2).

NETs, defined by the result of triple staining ($CD15^+/MPO^+/H3Cit^+$), appear as white co-stained structures (Figures 1–4), quantified as area percentage. Using this parameter, a marked level of heterogeneity among cases of each disease was found, as indicated by prominent coefficients of variation (Figure 2). This is illustrated by cases with lower and higher densities of NETs in representative images corresponding to each disease (Figure 2).

These results show the presence of NETs in human solid tumours. Importantly, not all tumour-infiltrating neutrophils form H3Cit NETs. However, the density of neutrophil infiltration strongly correlated with the percentage of NET area (see supplementary material, Figure S2A–F), indicating a relationship between neutrophil entrance to cancer tissue and NETosis.

Associations of tumour NETs with IL-8 and reduced $CD8^+$ T-cell infiltrates

Our previous mouse model work suggested that NETs interfere with $CD8^+$ T-cell infiltrates and function in engrafted tumours [13]. Therefore, we added CD8 staining to the multiplex panel. Furthermore, we recently set up a method for multiplex immunostaining of IL-8 at the protein level [35] that could be used in sequential sections.

Using these protocols, we analysed TMAs of NSCLC and bladder cancer. A series of tissue sections of melanoma were also evaluated. The results shown in Figure 3 indicated a positive association between IL-8 protein expression and NETs area in these three tumours. Furthermore, the density of $CD8^+$ T lymphocytes negatively correlated with NET area, with the exception of melanoma, where such a relationship was less pronounced. Local IL-8 protein expression did not correlate with $CD8^+$ T-cell infiltration in none of three tumour types studied (NSCLC: $r = 0.15$, $p = 0.60$; bladder cancer: $r = -0.43$, $p = 0.13$; melanoma: $r = 0.32$, $p = 0.41$).

Spatial variation of NET presence in cancer tissue

The results using melanoma whole tissue sections revealed areas with lower and higher density of NETs. Taking advantage of this fact, large tumour areas were divided into 250×250 μm^2 tiles clearly indicating heterogeneous distribution, as shown by a representative case in Figure 4A and quantitative data of the tiles in four melanoma cases with NET content (Figure 4B).

Interestingly, NETs seemed to be more abundant in and around areas of tumour cell necrosis, as shown by H&E staining of serial contiguous sections (Figure 4A). Using the tiles from the four melanoma cases, we found a negative correlation between the density of NETs in each tile and the density of $CD8^+$ T lymphocytes.

Circulating NETs correlate with serum IL-8 concentrations in melanoma and NSCLC

The presence and abundance of NETs in circulation could be capturing the formation of NETs in the tumour or elsewhere in the body of the tumour-bearing patient.

We set up three quantitative ELISA methods to unequivocally evaluate the presence of NETs in serum (see supplementary material, Figure S1A). As positive controls and standards, we used NETs induced in isolated neutrophils from healthy donors and cancer patients with PMA or IL-8 [40], rendering linear ranges of quantitative detection based on simultaneous

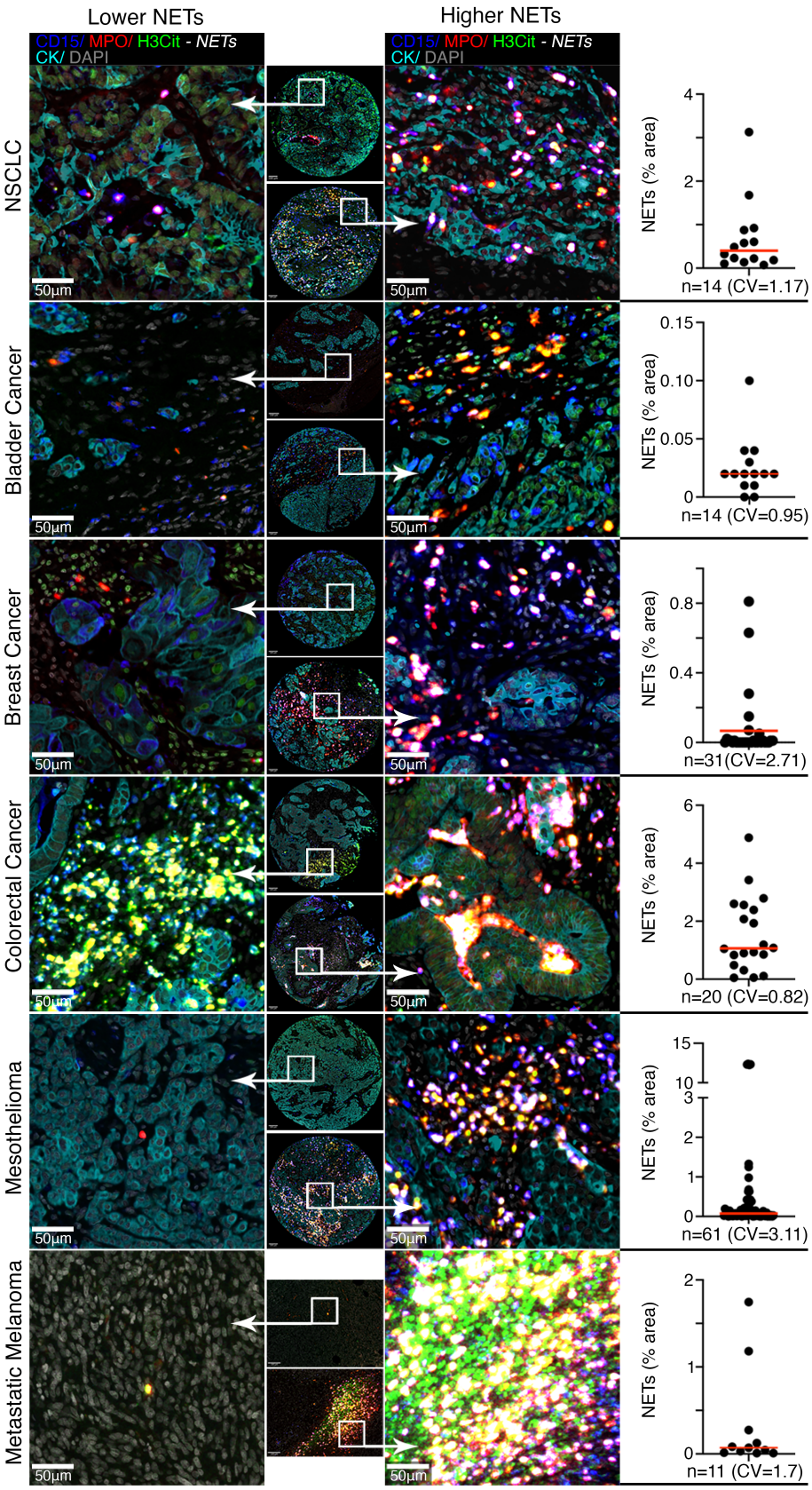

Figure 2. Identification and quantification of NET and neutrophils forming NETs in human solid tumours. Full composite images of representative cases with lower and higher NETs from NSCLC, bladder cancer, breast cancer, CRC, mesothelioma and metastatic melanoma. Higher magnifications from the composite images are displayed, as shown. NETs are identified by triple marker immunostaining: CD15 (blue), MPO (red) and anti-histone H3 (citrulline R2+R8+R17, H3Cit, green), and are visualised as white structures in the full composite images. Tumour cells are shown in cyan and cell nuclei in grey. Tissue density (% area) of NET and neutrophils forming NETs and the coefficient of variation (CV) are shown for all tumour types. Scale bars, 50 µm.

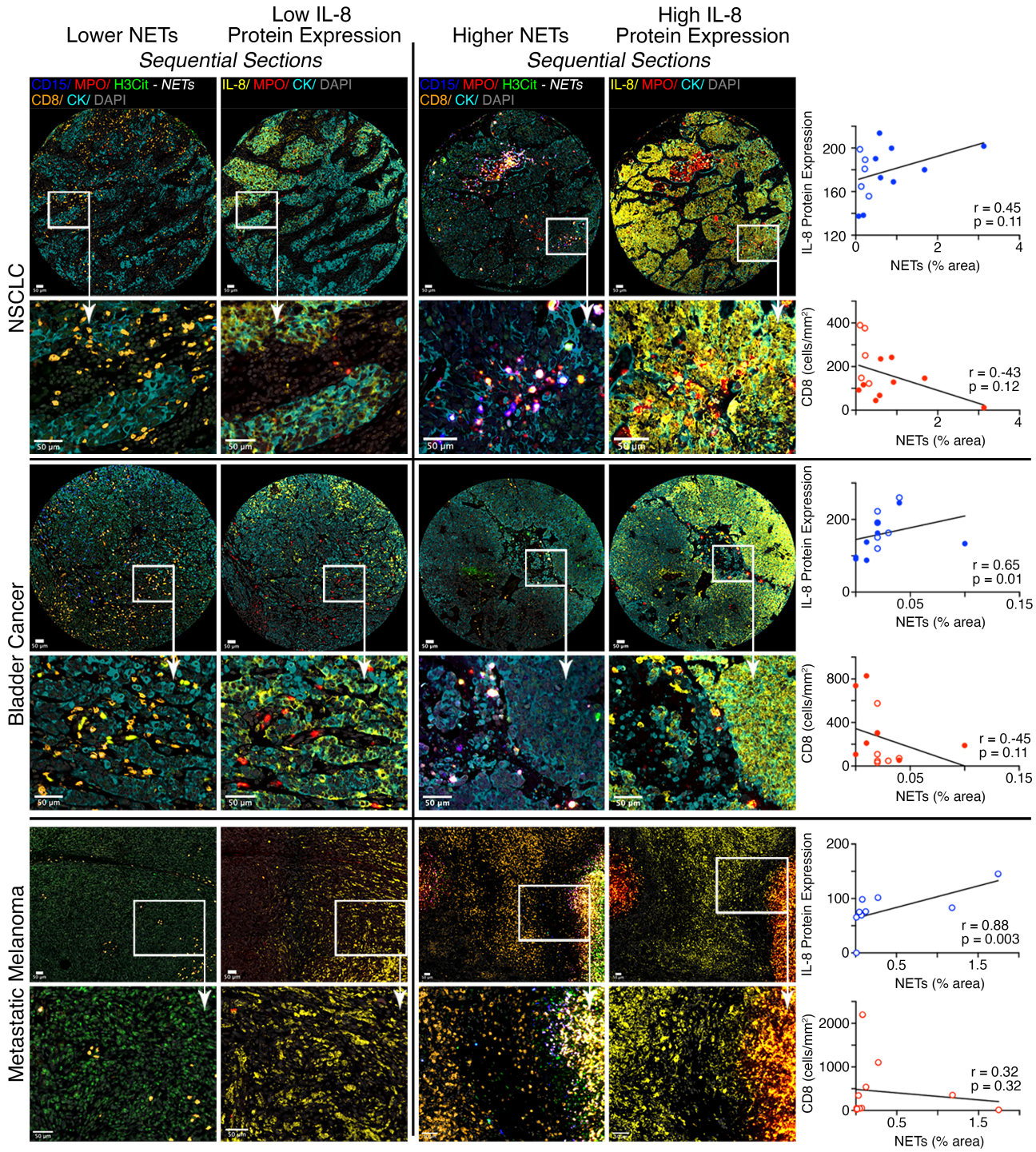

Figure 3. NET association with IL-8 protein expression and $CD8^+$ T-cell density in NSCLC, bladder cancer and metastatic melanomas. Full composite images of cases with lower NETs and low IL-8 protein expression and higher NETs and high IL-8 protein expression. Sequential tissue sections are shown. As indicated, regions of interests are shown at higher magnifications for each representative tumour images. Scatter plots measuring the degree of correlation between variables, NETs, $CD8^+$ T-cell density and IL-8 protein expression are shown. Spearman correlation coefficient and *P* value are shown for all relationships. Filled circles indicate primary cases; circles indicate metastatic cases (see supplementary material, Table S1). Scale bars, 50 µm.

antibody binding to dsDNA, H3Cit or MPO in sandwich ELISA pairs (see supplementary material, Figure S1A).

These ELISA methods were used in retrospective serum sample collections of melanoma (Figure 5A) and NSCLC (Figure 5B) cases with high tumour burden. The correlation among the ELISA methods on these samples is shown in supplementary material, Figure S1B.

NET serum concentration showed prominent levels of interindividual variability (Figure 5) that we correlated with the circulating concentration of IL-8 (Figure 5A, B) to show a positive association between these two

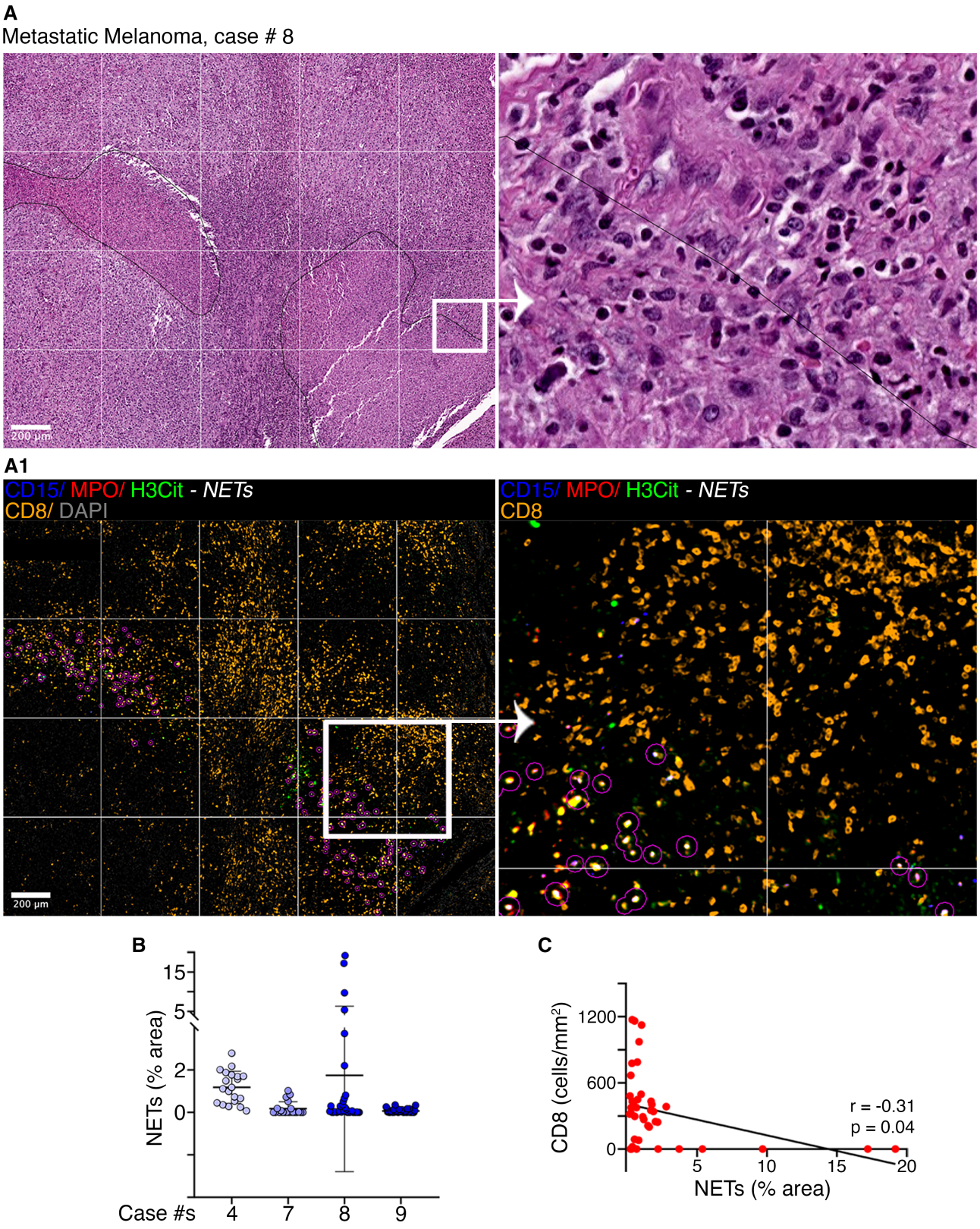

Figure 4. Spatial variation of NETs in whole tissue sections from melanomas. (A) Sequential tissue sections of a representative case of metastatic melanoma (case #8) stained with H&E and with multiplex immunofluorescence targeting NETs CD15, blue; MPO, red; and anti-histone H3 (citrulline R2+R8+R17, H3Cit, green) and $CD8^+$ T cells (orange). NETs are identified by triple marker immunostaining: CD15, MPO and H3Cit, and are visualised as white structures in the full composite images (magenta circles). On the H&E slide, areas with neutrophils are indicated by the black line. For the quantification of NETs and $CD8^+$ T cells on each multiplex immunofluorescence image, a grid of tiles (each tile: 250 × 250 μm^2) covering the whole tissue section was applied. (B) NET densities (% area) from the cases with detectable NETs are shown. Each dot represents a tile area. Mean values are indicated by a black dash. (C) Scatter plot measuring the degree of correlation between NETs and $CD8^+$ T-cell densities in each tile area. Spearman correlation coefficient and *P* values are shown. Scale bars, 200 µm.

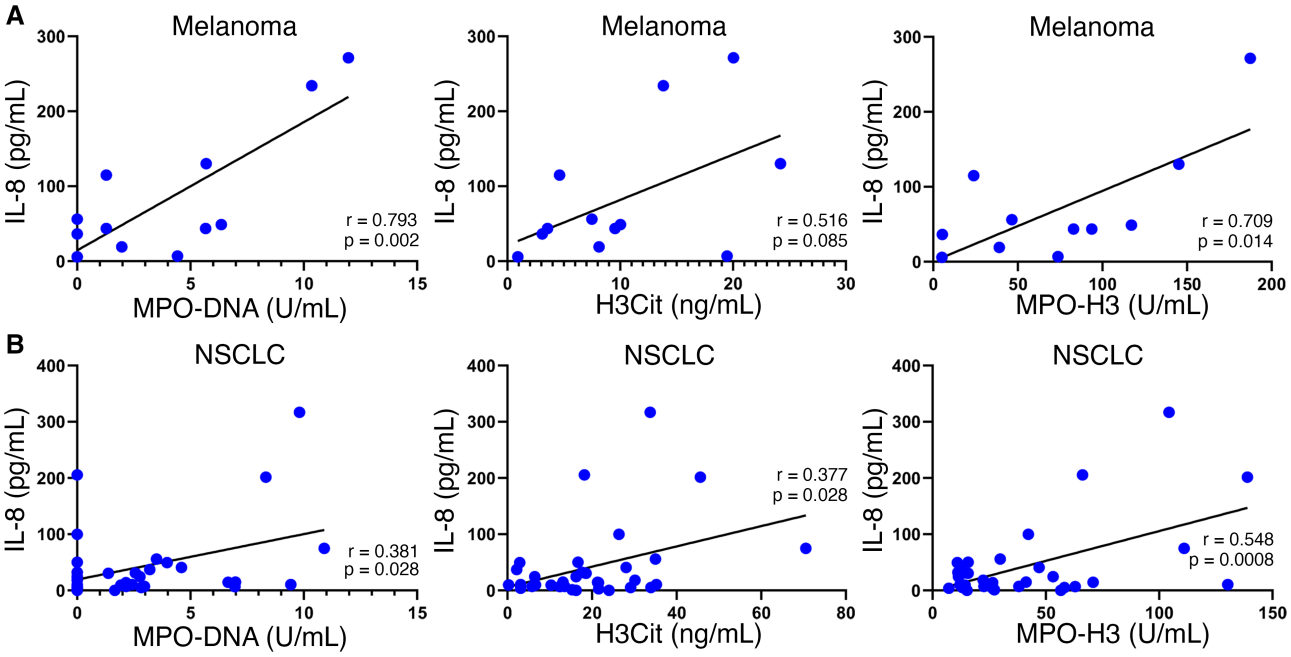

Figure 5. Serum IL-8 concentrations correlate with NETs in melanoma and NSCLC patients. Scatter plot measuring the degree of correlation between IL-8 concentrations and NETs measured in serum as complexes of MPO-DNA, H3Cit and complexes of MPO-histone 3. (A,B) The measurements were carried out in serum of metastatic melanoma ($n = 12$) and NSCLC ($n = 34$) patients. MPO-DNA and MPO-3H complexes are quantified in units referred to a standard made with NETs produced *in vitro* by neutrophils activated with IL-8. Spearman correlation coefficient and *P* values are shown.

parameters, when measuring NETs by the three ELISA methods and IL-8 concentrations by a commercial sandwich ELISA. All in all, NETs are detectable in the circulation of patients with solid malignancies with a broad variation that seems to correlate to some extent with circulating IL-8.

Discussion

This study offers unambiguous evidence for NETosis in human cancer. According to mouse models, NETs are elements that exacerbate cancer progression through multiple mechanisms [15,41]. Neutrophils in these experimental settings and in cancer patients are perceived as pro-cancer elements, even though there is some controversy regarding other putative anticancer mechanisms mediated by neutrophils [42–44].

Our multiplex immunofluorescence methodology detects and quantitates NETs and neutrophils forming NETs in human tissue. Importantly, our methodology offers *(i)* robust analytical validation of the assay that can be used to analyse clinically relevant FFPE samples, *(ii)* automated quantitative analysis, and *(iii)*, the possibility for spatial analysis.

Previous reports on single parameter staining indicated that the abundance of NETs in lymphoma as well as pancreatic and ovarian cancer, correlates with worse overall prognosis [19–21]. Mouse data are supportive of pathogenic mechanisms exerted by NETs, but this remains unresolved in humans. One of the most prominent factors that elicits NETosis on human neutrophils is IL-8 acting on CXCR1 and CXCR2 [14,17]. Such a function cannot be addressed in mice as IL-8 is absent from the genome of rodents, precluding direct preclinical experiments. In our hands, IL-8 immunostaining shows positive association with NETs, suggesting that this factor is involved, although other mediators enriched in the tumour microenvironment probably also contribute [15]. Such a correlation is also found between serum IL-8 concentrations and NET presence in the circulation. Whether circulating NETs play a pathogenic role remains to be seen, but our previous work in mice suggests that NETs in the circulation may protect metastasising tumour cells from immune-mediated cytotoxicity [13]. Furthermore, NETs are probably important in the premetastatic niche conditioning the organ soil to accept the metastatic seeds [10,45]. In this sense, circulating NETs could reflect such metastasis propensity that is upregulated in mice by systemic inflammation [46].

It is very important to consider that wide variability is observed among individual cases of multiple human cancer types, both in tissue and in serum. This offers a great opportunity for correlative studies [47], which we have started in a prospective manner given the fact that our present report has the limitation of working on retrospective series.

Heterogeneity is also spatial within a given tumour for reasons that are unclear, but may be related to hypoxia and necrosis. Other potential factors are heterogeneous expression of proinflammatory factors such as TNF, IL-17 or IL-1β, known to induce IL-8 [48] as well as other NET inducers (I Olivera, University of Navarra, personal communication 2021).

Another intriguing conclusion of our studies is the inverse correlation between $CD8^+$ T cells and NETs. This suggests that NETs could be impairing CD8-mediated antitumour immunity [13,48]. This has relevance in cancer immunotherapy, both as a putative biomarker and because it would allow actionable targets to be identified. Indeed, neutrophils and IL-8 have been shown to negatively correlate with clinical benefit from checkpoint inhibitors [18,35,49,50]. Clinical trials testing CXCR1/2 inhibitors and IL-8 blocking antibodies in combination with anti-PD(L)1 agents are in progress or about to begin [51,52].

The non-immune effects of IL-8 and NETs can also be important to foster metastasis and cancer progression, including their actions in the premetastatic niche [10,14]. The detection of NETs in the circulation, which probably represents overall NETosis levels in patients, may be complementary to tissue determinations, compensating for spatial heterogeneity in the manner that liquid biopsies do.

All things considered, conclusive evidence for the presence and individual variation of NETs in human cancer sets the stage for prospective or retrospective correlative studies with prognosis and response to immune and non-immune therapies.

Acknowledgements

We are grateful to Drs A Gonzalez, I Gil-Bazo, A Gurpide, SM Algarra, for their long-term support and helpful discussions. Excellence in nursing performance and blood sample collection by MP Andueza and L Resano is also acknowledged. This project has been supported by grants from the I-ON program from Bristol-Myers Squibb, Partners of Choice Network from AstraZeneca, MINECO SAF2017-83267-C2-1-R (AEI/FEDER, UE) and Instituto de Salud Carlos III and co-financed by Fondos FEDER. This project has also received funding from the European Union's Horizon 2020 Research and Innovation Program (grant agreement no. 635122 - PROCROP), Fundación de la Asociación Española Contra el Cancer (AECC) and Cancer Research UK (Accelerator Project: Local Radioimmunotherapy). AT has received financial support through 'la Caixa' Banking Foundation (LCF/BQ/LR18/11640014). COS has received financial support through the Spanish Ministry of Science, Innovation and Universities, under grants RTI2018-094494-B-C22 and RTC-2017-6218-1 (MCIU/AEI/FEDER, UE). MFS is supported by a Miguel Servet contract from Instituto de Salud Carlos III, Fondo de Investigacion Sanitaria (Spain).

Author contributions statement

CEA, JLPG, MERR, KAS, MFS and IM conceived the study. MCO, MV and AT designed the experiments. MAM, IK, CS, SS, SG, MA, COS, MDL and JIE produced and analysed the data, and contributed to data interpretation. CEA, KAS, AT, MFS and IM wrote the manuscript with input from all authors.

References

1. Brinkmann V, Reichard U, Goosmann C, *et al*. Neutrophil extracellular traps kill bacteria. *Science* 2004; **303:** 1532–1535.
2. Branzk N, Lubojemska A, Hardison SE, *et al*. Neutrophils sense microbe size and selectively release neutrophil extracellular traps in response to large pathogens. *Nat Immunol* 2014; **15:** 1017–1025.
3. Papayannopoulos V. Neutrophil extracellular traps in immunity and disease. *Nat Rev Immunol* 2018; **18:** 134–147.
4. Fuchs TA, Brill A, Duerschmied D, *et al*. Extracellular DNA traps promote thrombosis. *Proc Natl Acad Sci U S A* 2010; **107:** 15880–15885.
5. Schauer C, Janko C, Munoz LE, *et al*. Aggregated neutrophil extracellular traps limit inflammation by degrading cytokines and chemokines. *Nat Med* 2014; **20:** 511–517.
6. Muñoz LE, Boeltz S, Bilyy R, *et al*. Neutrophil extracellular traps initiate gallstone formation. *Immunity* 2019; **51:** 443–450.e4.
7. Kessenbrock K, Krumbholz M, Schönermarck U, *et al*. Netting neutrophils in autoimmune small-vessel vasculitis. *Nat Med* 2009; **15:** 623–625.
8. Yu M, Li T, Li B, *et al*. Phosphatidylserine-exposing blood cells, microparticles and neutrophil extracellular traps increase procoagulant activity in patients with pancreatic cancer. *Thromb Res* 2020; **188:** 5–16.
9. Jung HS, Gu J, Kim JE, *et al*. Cancer cell-induced neutrophil extracellular traps promote both hypercoagulability and cancer progression. *PLoS One* 2019; **14:** e0216055.
10. Cools-Lartigue J, Spicer J, McDonald B, *et al*. Neutrophil extracellular traps sequester circulating tumor cells and promote metastasis. *J Clin Invest* 2013; **123:** 3446–3458.
11. Yang L, Liu Q, Zhang X, *et al*. DNA of neutrophil extracellular traps promotes cancer metastasis via CCDC25. *Nature* 2020; **583:** 133–138.
12. Albrengues J, Shields MA, Ng D, *et al*. Neutrophil extracellular traps produced during inflammation awaken dormant cancer cells in mice. *Science* 2018; **361:** eaao4227.
13. Teijeira Á, Garasa S, Gato M, *et al*. CXCR1 and CXCR2 chemokine receptor agonists produced by tumors induce neutrophil extracellular traps that interfere with immune cytotoxicity. *Immunity* 2020; **52:** 856–871.e8.
14. Alfaro C, Sanmamed MF, Rodríguez-Ruiz ME, *et al*. Interleukin-8 in cancer pathogenesis, treatment and follow-up. *Cancer Treat Rev* 2017; **60:** 24–31.
15. Teijeira A, Garasa S, Ochoa MC, *et al*. IL8, neutrophils, and NETs in a collusion against cancer immunity and immunotherapy. *Clin Cancer Res* 2021; **27:** 2383–2393.
16. Moore BB, Kunkel SL. Attracting attention: discovery of IL-8/CXCL8 and the birth of the chemokine field. *J Immunol* 2019; **202:** 3–4.
17. Teijeira A, Garasa S, Ochoa MDC, *et al*. Differential interleukin-8 thresholds for chemotaxis and netosis in human neutrophils. *Eur J Immunol* 2021. https://doi.org/10.1002/eji.202049029 [Epub ahead of print].
18. Jaillon S, Ponzetta A, Di Mitri D, *et al*. Neutrophil diversity and plasticity in tumour progression and therapy. *Nat Rev Cancer* 2020; **20:** 485–503.
19. Nie M, Yang L, Bi X, *et al*. Neutrophil extracellular traps induced by IL8 promote diffuse large B-cell lymphoma progression via the TLR9 signaling. *Clin Cancer Res* 2019; **25:** 1867–1879.
20. Jin W, Xu HX, Zhang SR, *et al*. Tumor-infiltrating NETs predict postsurgical survival in patients with pancreatic ductal adenocarcinoma. *Ann Surg Oncol* 2019; **26:** 635–643.

21. Zhang Y, Hu Y, Ma C, *et al*. Diagnostic, therapeutic predictive, and prognostic value of neutrophil extracellular traps in patients with gastric adenocarcinoma. *Front Oncol* 2020; **10:** 1036.
22. Hisada Y, Grover SP, Maqsood A, *et al*. Neutrophils and neutrophil extracellular traps enhance venous thrombosis in mice bearing human pancreatic tumors. *Haematologica* 2020; **105:** 218–225.
23. Grilz E, Mauracher LM, Posch F, *et al*. Citrullinated histone H3, a biomarker for neutrophil extracellular trap formation, predicts the risk of mortality in patients with cancer. *Br J Haematol* 2019; **186:** 311–320.
24. Rodrigues MR, Rodriguez D, Russo M, *et al*. Macrophage activation includes high intracellular myeloperoxidase activity. *Biochem Biophys Res Commun* 2002; **292:** 869–873.
25. Bilusic M, Heery CR, Collins JM, *et al*. Phase I trial of HuMax-IL8 (BMS-986253), an anti-IL-8 monoclonal antibody, in patients with metastatic or unresectable solid tumors. *J Immunother Cancer* 2019; **7:** 240.
26. Goldstein LJ, Perez RP, Yardley D, *et al*. A window-of-opportunity trial of the CXCR1/2 inhibitor reparixin in operable HER-2-negative breast cancer. *Breast Cancer Res* 2020; **22:** 4.
27. Lewis HD, Liddle J, Coote JE, *et al*. Inhibition of PAD4 activity is sufficient to disrupt mouse and human NET formation. *Nat Chem Biol* 2015; **11:** 189–191.
28. Yang C, Montgomery M. Dornase alfa for cystic fibrosis. *Cochrane Database Syst Rev* 2018; **9:** CD001127.
29. Datar I, Sanmamed MF, Wang J, *et al*. Expression analysis and significance of PD-1, LAG-3, and TIM-3 in human non-small cell lung cancer using spatially resolved and multiparametric single-cell analysis. *Clin Cancer Res* 2019; **25:** 4663–4673.
30. Elgendy M, Fusco JP, Segura V, *et al*. Identification of mutations associated with acquired resistance to sunitinib in renal cell cancer. *Int J Cancer* 2019; **145:** 1991–2001.
31. Cienfuegos JA, Rodríguez J, Baixauli J, *et al*. Neoadjuvant chemotherapy without radiotherapy for patients with locally advanced rectal cancer. Oncologic outcomes. *Rev Esp Enferm Dig* 2020; **112:** 16–22.
32. Camp RL, Chung GG, Rimm DL. Automated subcellular localization and quantification of protein expression in tissue microarrays. *Nat Med* 2002; **8:** 1323–1327.
33. Abengozar-Muela M, Esparza MV, Garcia-Ros D, *et al*. Diverse immune environments in human lung tuberculosis granulomas assessed by quantitative multiplexed immunofluorescence. *Mod Pathol* 2020; **33:** 2507–2519.
34. Salas-Benito D, Conde E, Tamayo-Uria I, *et al*. The mutational load and a T-cell inflamed tumour phenotype identify ovarian cancer patients rendering tumour-reactive T cells from PD-1^{+} tumour-infiltrating lymphocytes. *Br J Cancer* 2021; **124:** 1138–1149.
35. Schalper KA, Carleton M, Zhou M, *et al*. Elevated serum interleukin-8 is associated with enhanced intratumor neutrophils and reduced clinical benefit of immune-checkpoint inhibitors. *Nat Med* 2020; **26:** 688–692.
36. Schmidt U, Weigert M, Broaddus C, *et al*. Cell detection with star-convex polygons. In *Medical Image Computing and Computer Assisted Intervention – MICCAI 2018. MICCAI 2018* Lecture Notes in Computer Science (Vol. 11071), Frangi A, Schnabel J, Davatzikos C, *et al*. (eds). Springer: London, 2018; 265–273.
37. McLaughlin J, Han G, Schalper KA, *et al*. Quantitative assessment of the heterogeneity of PD-L1 expression in non-small-cell lung cancer. *JAMA Oncol* 2016; **2:** 46–54.
38. Mohanan S, Cherrington BD, Horibata S, *et al*. Potential role of peptidylarginine deiminase enzymes and protein citrullination in cancer pathogenesis. *Biochem Res Int* 2012; **2012:** 895343.
39. McMillen TS, Heinecke JW, LeBoeuf RC. Expression of human myeloperoxidase by macrophages promotes atherosclerosis in mice. *Circulation* 2005; **111:** 2798–2804.
40. Alfaro C, Teijeira A, Oñate C, *et al*. Tumor-produced interleukin-8 attracts human myeloid-derived suppressor cells and elicits extrusion of neutrophil extracellular traps (NETs). *Clin Cancer Res* 2016; **22:** 3924–3936.
41. Masucci MT, Minopoli M, Del Vecchio S, *et al*. The emerging role of neutrophil extracellular traps (NETs) in tumor progression and metastasis. *Front Immunol* 2020; **11:** 1749.
42. Gershkovitz M, Caspi Y, Fainsod-Levi T, *et al*. TRPM2 mediates neutrophil killing of disseminated tumor cells. *Cancer Res* 2018; **78:** 2680–2690.
43. Hagerling C, Gonzalez H, Salari K, *et al*. Immune effector monocyte-neutrophil cooperation induced by the primary tumor prevents metastatic progression of breast cancer. *Proc Natl Acad Sci U S A* 2019; **116:** 21704–21714.
44. Cui C, Chakraborty K, Tang XA, *et al*. Neutrophil elastase selectively kills cancer cells and attenuates tumorigenesis. *Cell* 2021; **184:** 3163–3177.e21.
45. Lee W, Ko SY, Mohamed MS, *et al*. Neutrophils facilitate ovarian cancer premetastatic niche formation in the omentum. *J Exp Med* 2019; **216:** 176–194.
46. Rayes RF, Mouhanna JG, Nicolau I, *et al*. Primary tumors induce neutrophil extracellular traps with targetable metastasis promoting effects. *JCI Insight* 2019; **5:** e128008.
47. Perez-Gracia JL, Sanmamed MF, Bosch A, *et al*. Strategies to design clinical studies to identify predictive biomarkers in cancer research. *Cancer Treat Rev* 2017; **53:** 79–97.
48. Zhang Y, Chandra V, Riquelme Sanchez E, *et al*. Interleukin-17-induced neutrophil extracellular traps mediate resistance to checkpoint blockade in pancreatic cancer. *J Exp Med* 2020; **217:** e20190354.
49. Yuen KC, Liu LF, Gupta V, *et al*. High systemic and tumor-associated IL-8 correlates with reduced clinical benefit of PD-L1 blockade. *Nat Med* 2020; **26:** 693–698.
50. Sanmamed MF, Perez-Gracia JL, Schalper KA, *et al*. Changes in serum interleukin-8 (IL-8) levels reflect and predict response to anti-PD-1 treatment in melanoma and non-small-cell lung cancer patients. *Ann Oncol* 2017; **28:** 1988–1995.
51. ClinicalTrials.gov. Identifier NCT03400332. A Phase 1/2 Study of BMS-986253 in Combination With Nivolumab or Nivolumab Plus Ipilimumab in Advanced Cancers; 2018 February 12; 2021 May 11. Bethesda, MD: National Library of Medicine (US); [about 6 screens]. [Accessed 22 June 2021]. Available from: https://clinicaltrials.gov/ct2/show/NCT03400332
52. ClinicalTrials.gov. Identifier NCT03177187. ACE: Proof of Concept Phase I/II Trial of the CXCR2 Antagonist AZD5069, Administered in Combination With Enzalutamide, in Patients With Metastatic Castration Resistant Prostate Cancer (mCRPC); 2017 November 13; 2021 May 3. Bethesda, MD: National Library of Medicine (US); [about 6 screens]. [Accessed 22 June 2021]. Available from: https://clinicaltrials.gov/ct2/show/NCT03177187

SUPPLEMENTARY MATERIAL ONLINE

Figure S1. Three different methods used to determine NET quantities in serum

Figure S2. Neutrophil and NET density correlations in tumour tissue

Table S1. Clinicopathological characteristics of the patients included in this study